RMetS
Royal Meteorological Society

The advection–condensation model and water-vapour probability density functions

Jai Sukhatme,[a]* and William R. Young[b]

[a]*Centre for Atmospheric and Oceanic Sciences, Indian Institute of Science, Bangalore 560012, India*
[b]*Scripps Institute of Oceanography, University of California at San Diego, San Diego, CA 92093-0213, USA.*
*Correspondence to: J. Sukhatme, Centre for Atmosphere and Oceanic Sciences, Indian Institute of Science, Bangalore, Karnataka 560012, India. E-mail: jai.goog@gmail.com

The statistically steady humidity distribution resulting from an interaction of advection, modelled as an uncorrelated random walk of moist parcels on an isentropic surface, and a vapour sink, modelled as immediate condensation whenever the specific humidity exceeds a specified saturation humidity, is explored with theory and simulation. A source supplies moisture at the deep-tropical southern boundary of the domain and the saturation humidity is specified as a monotonically decreasing function of distance from the boundary. The boundary source balances the interior condensation sink, so that a stationary spatially inhomogeneous humidity distribution emerges. An exact solution of the Fokker–Planck equation delivers a simple expression for the resulting probability density function (PDF) of the water-vapour field and also the relative humidity. This solution agrees completely with a numerical simulation of the process, and the humidity PDF exhibits several features of interest, such as bimodality close to the source and unimodality further from the source. The PDFs of specific and relative humidity are broad and non-Gaussian. The domain-averaged relative humidity PDF is bimodal with distinct moist and dry peaks, a feature which we show agrees with middleworld isentropic PDFs derived from the ERA interim dataset.

Key Words: diffusion; relative humidity; specific humidity; bimodal

Received 29 November 2010; Revised 7 April 2011; Accepted 23 May 2011; Published online in Wiley Online Library

Citation: Sukhatme J, Young WR. 2011. The advection–condensation model and water-vapour probability density functions. *Q. J. R. Meteorol. Soc.* DOI:10.1002/qj.869

1. Introduction

Water vapour plays a significant role in diverse problems pertaining to the dynamics of the Earth's climate (Pierrehumbert, 2002; Schneider *et al.*, 2010). In particular, with regards to its radiative effects, estimating the amount of water vapour in the upper troposphere is crucial (Spencer and Braswell, 1997; Held and Soden, 2000). Significant efforts–especially directed towards the subtropical troposphere–have yielded a key insight into the non-local nature of processes that control the distribution of water vapour (Yang and Pierrehumbert, 1994; Sherwood, 1996; Salathe and Hartman, 1997; Pierrehumbert, 1998; Pierrehumbert and Roca, 1998; Galewsky *et al.*, 2005; Brogniez *et al.*, 2009).

The resultant framework for understanding the evolution of water vapour, or generally any condensable substance in a fluid dynamical setting, is known as the advection–condensation (AC) model. The recent review by Sherwood *et al.* (2009) provides an introduction, while the book chapter by Pierrehumbert *et al.* (2005) (hereafter PBR) provides a thorough overview of the AC model.

Further, as elaborated on by Spencer and Braswell (1997) and PBR, in addition to the amount, the probability density function (PDF) of the water-vapour field has a strong influence on the long-wave cooling of the atmosphere. Explicit calculations illustrating the effect of the PDF on the outgoing long-wave radiation (OLR) are given by Zhang *et al.* (2003). The importance of the PDF stems from the approximately logarithmic dependence of the change in OLR

to the specific humidity of the water vapour in the domain. Further discussion of this logarithmic dependence, which results from a spectral broadening of absorption peaks, can be found in the text by Pierrehumbert (2010).

Following Soden and Bretherton (1993), there have been numerous efforts that examine water-vapour PDFs in the tropical and subtropical troposphere. A principal feature noted by these studies is the non-normality of the PDFs. A range of distributions, from bimodality in the deep Tropics (Brown and Zhang, 1997; Zhang *et al.*, 2003; Mote and Frey, 2006; Luo *et al.*, 2007) to unimodal PDFs with a roughly log-normal or power-law form in the subtropics have been documented (Soden and Bretherton, 1993; Sherwood *et al.*, 2006). Ryoo *et al.* (2009) have emphasized that a salient and baffling feature of water-vapour PDFs is their spatial inhomogeneity. Models based on the statistics of subsidence drying and random re-moistening of parcels reproduce many of the observed features of the humidity PDFs, provided that one considers the model parameters to be functions of position determined to match observations (Sherwood *et al.*, 2006; Ryoo *et al.*, 2009).

One of the main achievements of this article is an exact solution for the water-vapour PDF that characterizes the statistically steady state emerging from an interaction of advection, condensation and a spatially localized moisture source. In particular, we consider moist parcels advected by a white-noise stochastic velocity field. Each parcel carries a specific humidity and experiences condensation whenever and wherever the specific humidity exceeds a specified saturation profile. The parcel humidity is reset to saturation by a moist source at the southern boundary of the domain. In the ultimate statistically steady state, the southern vapour source is balanced by condensation throughout the interior of the domain. In contrast to earlier considerations of the AC model with white-noise advection (O'Gorman and Schneider, 2006), we consider statistically steady states rather than the initial value problem and we obtain the full water-vapour PDF rather than the mean humidity.

The AC model is described in more detail in sections 2 and 3 and in section 4 we solve the Fokker–Planck equation to obtain the PDF of the specific humidity. The utility of the PDF is demonstrated by calculating the average moisture flux and condensation. In section 5 we focus on a particular saturation profile–the standard exponential model–and exhibit analytical solutions for the specific and relative humidity PDFs; these are shown to be in very good agreement with PDFs estimated from a Monte Carlo simulation. In section 6 we analyze daily isentropic relative humidity data from the ERA interim product, and show that the PDFs derived from this dataset agree with the principal features predicted by our idealized model. A discussion of the PDFs, with implications for the atmospheric radiation budget and the present-day distribution of water vapour, followed by a conclusion in section 7 ends the article.

2. The AC model

The central quantity in the AC model is the specific humidity, defined by

$$q(\mathbf{x},\mathrm{t}) \stackrel{\text{def}}{=} \frac{\text{mass of water vapour in a parcel}}{\text{total mass of the parcel}}\,, \qquad (1)$$

where $\mathbf{x} = (\mathrm{x},\mathrm{y})$ is the position on an isentropic surface. Our main focus here is the extratropical vapour distribution, which is determined in large part by the wandering of air parcels on isentropic surfaces and the temperature changes associated with latitudinal excursions.

Following PBR, the AC model is

$$\partial_t q + \mathbf{u}\cdot\nabla q = \mathcal{S} - \mathcal{C}\,. \qquad (2)$$

Above, $\mathcal{S}$ is the vapour source, $\mathcal{C}$ is the condensation sink and $\mathbf{u}(\mathbf{x},\mathrm{t})$ is the velocity on an isentropic surface. In the absence of sources and sinks, $\mathrm{D}q/\mathrm{D}t = 0$, i.e. the specific humidity is a materially conserved quantity. The AC formalism does not consider the diffusive homogenization of water vapour, e.g. via the addition of $\chi\nabla^2 q$ on the right of (2). This limitation of the model is discussed further in section 6.

Latent heat release and radiative cooling result in significant cross-isentropic motion in the troposphere, and we have ignored this process in formulating a two-dimensional isentropic model in (2). We emphasize that the AC formulation is not inherently limited to two dimensions or to motion on isentropic surfaces. For ease of exposition and simplicity, however, isentropic motion is a useful starting point.

The condensation sink on the right of (2) might be modelled with

$$\mathcal{C} = \tau_{\mathrm{c}}^{-1}\left[q(\mathbf{x},\mathrm{t}) - q_{\mathrm{s}}(\mathbf{x})\right] H\left[q(\mathbf{x},\mathrm{t}) - q_{\mathrm{s}}(\mathbf{x})\right], \qquad (3)$$

where τ_{c} is the time-scale associated with condensation, $q_{\mathrm{s}}(\mathbf{x})$ is the prescribed saturation specific humidity and $H(x)$ denotes the Heaviside step function, which is zero if $x < 0$ and unity if $x > 0$. Observed atmospheric supersaturations rarely exceed a few per cent and therefore the sink $\mathcal{C}$ is extremely effective (Wallace and Hobbs, 1977). In other words, we are concerned with the rapid-condensation limit $\tau_{\mathrm{c}} \to 0$. In the rapid-condensation limit, the details in $\mathcal{C}$ are unimportant and condensation can instead be represented as a rule enforcing subsaturation:

$$q(\mathbf{x},\mathrm{t}) \to \min\left[q(\mathbf{x},\mathrm{t}), q_{\mathrm{s}}(\mathbf{x})\right]. \qquad (4)$$

Therefore $q(\mathbf{x},\mathrm{t}) \le q_{\mathrm{s}}(\mathbf{x})$ and there is an upper bound on the specific humidity at every $\mathbf{x}$. Globally, the maximum tolerable specific humidity is

$$q_{\max} \stackrel{\text{def}}{=} \max_{\forall\mathbf{x}} q_{\mathrm{s}}(\mathbf{x})\,. \qquad (5)$$

If the flow is ergodic then a wandering parcel explores the entire domain and eventually encounters the driest regions with the smallest value of $q_{\mathrm{s}}(\mathbf{x})$. Thus, in the absence of sources (Sukhatme and Pierrehumbert, 2006, pers. comm.),

$$\lim_{t\to\infty} q(\mathbf{x},\mathrm{t}) = q_{\min}\,, \qquad (6)$$

where

$$q_{\min} \stackrel{\text{def}}{=} \min_{\forall\mathbf{x}} q_{\mathrm{s}}(\mathbf{x})\,. \qquad (7)$$

On the other hand, without advection the source will eventually saturate $q(\mathbf{x},\mathrm{t})$ at every point $\mathbf{x}$ where $\mathcal{S} \neq 0$. Therefore, interesting statistically steady states are expected only if there is both a source $\mathcal{S}$ and advection $\mathbf{u}(\mathbf{x},\mathrm{t})$.

The problem is to determine the evolution and the statistics of the specific humidity $q(\mathbf{x},\mathrm{t})$, given the velocity field $\mathbf{u}(\mathbf{x},\mathrm{t})$ and the saturation profile $q_{\mathrm{s}}(\mathbf{x})$. Due to its

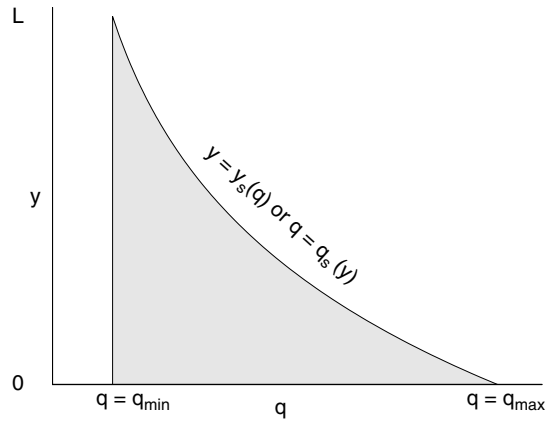

Figure 1. In the rapid-condensation limit the accessible domain in the (q, y) plane is the shaded region shown above. The model assumes that $q_s(y)$ decreases monotonically from $q_{max} = q_s(0)$ to $q_{min} = q_s(L)$. The functions $q_s(y)$ and $y_s(q)$ are inverses of each other: $q_s[y_s(q)] = q$.

physical significance, the principal statistical feature we focus here on is the probability density function (PDF) of q. Quantities such as the mean moisture flux and the mean condensation rate are also crucial, and have been examined in the AC framework (O'Gorman and Schneider, 2006; O'Gorman *et al.*, 2011). These mean quantities can be deduced from the PDF of q via integration over q.

3. Moist Brownian parcels

The simplest representation of random transport is obtained by taking the velocity $\mathbf{u}(\mathbf{x}, \mathrm{t})$ in (2) as having rapid temporal decorrelation so that the motion of an air parcel is Brownian. Then the spatial evolution of an ensemble of parcels, each carrying its own individual value of q, is described by the diffusion equation. We also assume that q_s depends only on the meridional coordinate y in the domain $0 < y < L$, and that q_s decreases monotonically from q_{max} at $y = 0$ to q_{min} at $y = L$. Each parcel is located at a point in the configuration space (q, y). Because of the condensation rule (4), the ensemble of parcels is confined to the shaded region of configuration space illustrated in Figure 1.

The AC model is then expressed as a set of coupled stochastic differential equations governing the position $Y(t)$ and specific humidity $Q(t)$ of a moist Brownian parcel:

$$\begin{aligned} \mathrm{d}Y(t) &= \sqrt{2\kappa_\mathrm{b}}\,\mathrm{d}W(t), \\ \mathrm{d}Q(t) &= \{\mathcal{S}\,[Y(t)] - \mathcal{C}\,[Y(t), Q(t)]\}\;\mathrm{d}t, \end{aligned} \tag{8}$$

where $W(t)$ is a Weiner process, κ_b is the Brownian diffusivity associated with the random walk and $\mathcal{S}$ and $\mathcal{C}$ are the source and condensation functions in (2). The numerical simulations described below amount to Euler–Maruyama discretization of (8). The midlatitude baroclinic eddies responsible for transport have non-trivial spatio-temporal correlations (Sukhatme, 2005; O'Gorman and Schneider, 2006). Thus the white-noise advection used in (8) and in earlier AC studies is an idealization.

The statistical properties of the ensemble of moist Brownian parcels are characterized by a PDF $P(q, y, t)$, such that the expected number of parcels in $\mathrm{d}q\,\mathrm{d}y$ is equal to

$$N\,P(q, y, t)\,\mathrm{d}q\,\mathrm{d}y\,, \tag{9}$$

where N is the total number of parcels.

The evolution of $P(q, y, t)$ is governed by the Fokker–Planck equation

$$\partial_t P + \partial_q[(\mathcal{S} - \mathcal{C})P] = \kappa_\mathrm{b}\partial_y^2 P\,, \tag{10}$$

with the normalization

$$\int_0^L \int_{q_{min}}^{q_{max}} P(q, y, t)\,\mathrm{d}q\,\mathrm{d}y = 1\,. \tag{11}$$

In the limit of rapid condensation, as $q_{min} \le q(y, t) \le q_s(y)$, the normalization takes the form

$$\int_0^L \int_{q_{min}}^{q_s(y)} P(q, y, t)\,\mathrm{d}q\,\mathrm{d}y = 1\,. \tag{12}$$

Integrating $P(q, y, t)$ over q produces the marginal density

$$p(y, t) \stackrel{\mathrm{def}}{=} \int_{q_{min}}^{q_s(y)} P(q, y, t)\,\mathrm{d}q\,. \tag{13}$$

Because the Brownian motion of a parcel is independent of the specific humidity it carries, we expect that integration of (10) over q will show that $p(y, t)$ satisfies the diffusion equation, and indeed this result is immediate:

$$\partial_t p = \kappa_\mathrm{b}\partial_y^2 p\,. \tag{14}$$

If parcels are reflected back into the domain at $y = 0$ and L, then the solution of (14) is $\lim_{t\to\infty} p(y, t) = L^{-1}$. Thus if we seek long-time equilibrium solutions of the Fokker–Planck equation (10) then we require

$$L^{-1} = \int_{q_{min}}^{q_s(y)} P(q, y)\,\mathrm{d}q\,. \tag{15}$$

Note that the left of (15) is consistent with the global normalization in (11). In the limit $\tau_\mathrm{c} \to 0$, the steady, marginal normalization condition (15) applies at every y, and for all models of $\mathcal{S}$ and $\mathcal{C}$. In other words, in a statistical steady state the normalization condition (15) is equivalent to enforcing the rapid-condensation rule in (5). The normalization (15) figures prominently in the following solution of the Fokker–Planck equation. Similar 'variable limit' normalization conditions are encountered in the solution of integrate-and-fire neuron models (Fusi and Mattia, 1998).

4. Steady solution with 'resetting' at $y = 0$

Now we adopt a 'resetting' model for the vapour source $\mathcal{S}$: on encountering the southern boundary at $y = 0$, parcels are reflected back into the domain with a new value of q chosen from a specified probability density function $\Phi(q)$, with the normalization

$$\int_{q_{min}}^{q_{max}} \Phi(q)\,\mathrm{d}q = 1\,. \tag{16}$$

For example, completely saturating the parcels at $y = 0$ corresponds to the choice $\Phi(q) = \delta(q - q_{max})$. This is a simple representation of tropical moistening. The technique of resetting boundary conditions has been employed in a previous study of AC on isentropic surfaces (Yang and

Pierrehumbert, 1994), as well as in advection–diffusion of passive scalars (Pierrehumbert, 1994; Neufeld *et al.*, 2000).

We emphasize that resetting the humidity only at $y = 0$ is a strong model assumption that distinguishes this work from the AC models developed by Sherwood *et al.* (2006) and Ryoo *et al.* (2009). The statistical model developed in those works assumes that random resetting occurs throughout the domain as an exponential or gamma stochastic process with a characteristic time-scale $\tau_{\text{Moist}}(\mathbf{x})$. In effect, by resetting only at $y = 0$ we are considering the extreme case in which $\tau_{\text{Moist}}(\mathbf{x}) = \infty$ except at $y = 0$. Physically, the picture we have in mind is that parcels experience moistening when they encounter convective regions that are restricted to the Tropics, and therefore y is the distance from this saturated zone. In fact, this serves as another limiting case for the AC model along with the 're-setting throughout the domain' scenario considered by Sherwood *et al.* (2006) and Ryoo *et al.* (2009).

An important consequence of resetting only at $y = 0$ is that the driest parcels, which are created at $y = L$ with $q = q_{\min}$, maintain their extreme dryness till they eventually strike $y = 0$. The solution below requires explicit consideration of these driest parcels by inclusion of a component $\delta(q - q_{\min})$, referred to as the 'dry spike', in the PDF.

4.1. Solution of the Fokker–Planck equation

In the rapid-condensation limit, the accessible part of the (q, y) space is the shaded area in Figure 1, where $\mathcal{C} = 0$. With the resetting boundary condition, however, the source $\mathcal{S}$ is also zero within the shaded region. Thus the steady Fokker–Planck equation in the shaded region of Figure 1 collapses to $\partial_y^2 P = 0$, with the immediate solution

$$P(q, y) = \frac{\Phi(q)}{L} + yB(q)\,. \tag{17}$$

The first term on the right of (17) is determined by the resetting condition and by application of the normalization in (15) at $y = 0$.

Corresponding to the driest parcels in the domain, $B(q)$ in (17) must contain a component proportional to $\delta(q - q_{\min})$. This 'dry spike' contains parcels created by encounters with the northern boundary at $y = L$. These considerations refine (17) to

$$P(q, y) = \frac{\Phi(q)}{L} + \left[\frac{\delta(q - q_{\min})}{L^2} + F(q)\right] y\,. \tag{18}$$

The term $L^{-2}\delta(q - q_{\min})$ in (18) is obtained by applying the normalization condition (15) at $y = L$.

In (18), $F(q)$ is the smooth part of the PDF, which is determined by substituting into the normalization (15). This requirement leads to

$$\frac{L}{y}\int_{q_s(y)}^{q_{\max}} \Phi(q')\,\mathrm{d}q' = 1 + L^2 \int_{q_{\min}}^{q_s(y)} F(q')\,\mathrm{d}q'\,. \tag{19}$$

Inspecting (19), we see that it is possible to solve for $F(q)$ by using q, rather than y, as the independent variable. That is, following the notation in Figure 1, we use $y = y_s(q)$ to re-write (19) as

$$\frac{L}{y_s(q)}\int_{q}^{q_{\max}} \Phi(q')\,\mathrm{d}q' = 1 + L^2 \int_{q_{\min}}^{q} F(q')\,\mathrm{d}q'\,. \tag{20}$$

The derivative with respect to q then determines $F(q)$, i.e.

$$LF(q) = \frac{\mathrm{d}}{\mathrm{d}q}\frac{\Lambda(q)}{y_s(q)}\,, \tag{21}$$

where $\Lambda(q)$ is the cumulative distribution

$$\Lambda(q) \stackrel{\text{def}}{=} \int_{q}^{q_{\max}} \Phi(q')\,\mathrm{d}q'\,. \tag{22}$$

Assembling the pieces, we obtain the PDF

$$P(q, y) = -\frac{1}{L}\frac{\mathrm{d}\Lambda}{\mathrm{d}q} + \frac{y}{L}\left[\frac{\delta(q - q_{\min})}{L} + \frac{\mathrm{d}}{\mathrm{d}q}\frac{\Lambda(q)}{y_s(q)}\right]. \tag{23}$$

The expression above applies only within the shaded region in Figure 1 where $q < q_s(y)$; in the supersaturated region $q > q_s(y)$, $P(q, y) = 0$. The PDF is discontinuous at the saturation boundary $q = q_s(y)$. This completes the solution for the steady-state Fokker–Planck equation with resetting forcing at $y = 0$.

In summary, in the rapid-condensation limit, and with Brownian motion, the steady Fokker–Planck equation is solved exactly by (23). The normalization constraint in (15), and the use of q as the independent variable produces this relatively simple solution. In fact, the normalization constraint (15) can also be regarded as a differential boundary condition. Manipulating this boundary condition provides an alternate route to the solution, outlined in the Appendix.

4.2. The global PDF

The global PDF of specific humidity is the marginal density

$$g(q) \stackrel{\text{def}}{=} \int_{0}^{y_s(q)} P(q, y)\,\mathrm{d}y\,. \tag{24}$$

The integral on the right can be evaluated using the solution in (23), and one finds

$$g(q) = \frac{1}{2}\delta(q - q_{\min}) - \frac{1}{2}\frac{\mathrm{d}}{\mathrm{d}q}\left[y_s(q)\Lambda(q)\right]. \tag{25}$$

A comforting check on (25) is that $g(q)$ satisfies the normalization

$$\int_{q_{\min}}^{q_{\max}} g(q)\,\mathrm{d}q = 1\,, \tag{26}$$

which is consistent with (12).

Independent of model details, such as the specification of $q_s(y)$ and $\Lambda(q)$, the dry spike $\delta(q - q_{\min})$ in (25), contains exactly half of the parcels in the ensemble. Professor P. O'Gorman noted that this feature can be understood on the basis of symmetry: exactly half the parcels have more recently encountered the moist southern boundary than the dry northern boundary. The former half have $q \geq q_{\min}$, while the other half constitute the dry spike with $q = q_{\min}$.

4.3. Averages

Knowledge of the stationary PDF allows us to evaluate the average of any function of q, say $f(q)$, as

$$\langle f\rangle(y) \stackrel{\text{def}}{=} L\int_{q_{\min}}^{q_s(y)} f(q)P(q,y)\,\mathrm{d}q\,. \tag{27}$$

Using the solution for $P(q,y)$ in (23), one can show that the average defined above is

$$\langle f\rangle = f(q_s)\Lambda(q_s) - \int_{q_{\min}}^{q_s} f(q)\frac{\mathrm{d}\Lambda}{\mathrm{d}q}\,\mathrm{d}q - y\int_{q_{\min}}^{q_s}\frac{\mathrm{d}f}{\mathrm{d}q}\frac{\Lambda(q)}{y_s(q)}\,\mathrm{d}q\,. \tag{28}$$

Taking the derivative of (28) with respect to y, we obtain, after some remarkable cancellations,

$$\frac{\mathrm{d}\langle f\rangle}{\mathrm{d}y} = -\int_{q_{\min}}^{q_s}\frac{\mathrm{d}f}{\mathrm{d}q}\frac{\Lambda(q)}{y_s(q)}\,\mathrm{d}q\,. \tag{29}$$

4.4. Average humidity and condensation rate

To understand the transport of moisture in this model and the associated mean condensation rate, we return to (10) and momentarily retreat from the rapid-condensation limit*. Then, multiplying (10) by q and integrating from $q_{\min}$ to $q_{\max}$, we have

$$-\int_{q_s}^{q_{\max}} q\,\partial_q(\mathcal{C}P)\,\mathrm{d}q = \kappa_b\frac{\mathrm{d}^2\langle q\rangle}{\mathrm{d}y^2}\,, \tag{30}$$

where the condensation sink $\mathcal{C}$ is given by the model in (3). Using this expression for $\mathcal{C}$ and integrating the left of (30) by parts, we obtain the mean condensation rate defined by

$$\langle\mathcal{C}\rangle \stackrel{\text{def}}{=} \tau_c^{-1}\int_{q_s}^{q_{\max}}\big(q-q_s\big)\,P(q,y)\,\mathrm{d}q \tag{31}$$

as

$$\langle\mathcal{C}\rangle = \kappa_b\frac{\mathrm{d}^2\langle q\rangle}{\mathrm{d}y^2}\,. \tag{32}$$

The right-hand side of (32) is the convergence of the moisture flux, which balances the mean condensation $\langle\mathcal{C}\rangle$ on the left.

This argument shows that the flux of moisture has the same diffusivity κ_b as a Brownian parcel. As explained by O'Gorman and Schneider (2006), this is a special property of the Brownian limit: if the velocity has a non-zero integral time-scale (e.g. as in the Ornstein–Ulenbeck process) then the diffusivity of moisture will be systematically less than the random-walk diffusivity. We emphasize that while the moisture flux is diffusive, even with a Brownian advecting flow, the condensation sink cannot be adequately represented by a bulk diffusivity. This inadequacy of a mean-field representation of condensation is clearly demonstrated in PBR.

*We continue using resetting forcing, so that $\mathcal{S}=0$ when $y>0$.

In the rapid condensation limit, the right of (32) can be computed by putting $f(q)=q$ in (29). Thus if $\tau_c\to 0$, the mean condensation rate is

$$\langle\mathcal{C}\rangle = -\frac{\kappa_b}{y}\frac{\mathrm{d}q_s}{\mathrm{d}y}\,\Lambda\left(q_s(y)\right)\,. \tag{33}$$

Although $\mathcal{C}\propto\tau_c^{-1}\to\infty$, the mean condensation $\langle\mathcal{C}\rangle$ in (33) is independent of τ_c. This singular limit is achieved because the non-zero probability of supersaturation is confined to a boundary layer, lying just above the saturation boundary $q=q_s(y)$ in Figure 1.

If the resetting PDF $\Phi(q)$ is non-singular at $q_{\max}$, then $\langle\mathcal{C}\rangle$ in (33) is finite as $y\to 0$, despite the factor y^{-1}. Specifically, one can show that $\lim_{y\to 0}\Lambda(q_s)/y = -\Phi(q_{\max})(\mathrm{d}q_s/\mathrm{d}y)$.

5. An example

The solution from the previous section is most simply illustrated by supposing that the resetting produces complete saturation at $y=0$,

$$\Phi(q) = \delta(q-q_{\max})\,, \tag{34}$$

so that $\Lambda(q)=1$. For the saturation humidity we use the exponential model

$$q_s(y) = q_{\max}\,\mathrm{e}^{-\alpha y}\,. \tag{35}$$

This form of q_s has been employed previously in AC studies (Pierrehumbert *et al.*, 2005; O'Gorman and Schneider, 2006).

With $\Phi(q)$ and $q_s(y)$ in (34) and (35), the steady solution of the Fokker–Planck equation is

$$P(q,0) = \frac{\delta(q-q_{\max})}{L}\,, \tag{36}$$

and away from the southern boundary

$$P(q,0<y) = \frac{y}{L}\left[\frac{\delta(q-q_{\min})}{L} + \frac{\alpha}{q\log^2(q/q_{\max})}\right]. \tag{37}$$

The solution (37) can be non-dimensionalized with

$$\alpha_* \stackrel{\text{def}}{=} \alpha L\,,\qquad q_* \stackrel{\text{def}}{=} q/q_{\max}\,,\qquad y_* \stackrel{\text{def}}{=} y/L\,, \tag{38}$$

and $P_*(q_*,y_*) = q_{\max}LP(q,y)$. This scaling identifies the fundamental non-dimensional control parameter α_*, and the scaled PDF is

$$P_*(q_*,0<y_*) = y_*\left[\delta(q_*-\epsilon) + \frac{\alpha_*}{q_*\log^2(q_*)}\right], \tag{39}$$

with

$$\epsilon \stackrel{\text{def}}{=} \frac{q_{\min}}{q_{\max}} = \mathrm{e}^{-\alpha_*}\,. \tag{40}$$

At the southern boundary $P_*(q_*,0)=\delta(q_*-1)$. The main point is that the shape of $P_*(q_*,y_*)$ is controlled by a single parameter α_*.

There is an interesting change in the structure of P_* at $\alpha_*=2$: P_* is bimodal for all y_* if $\alpha_*<2$; if $\alpha_*>2$ then P_* is bimodal only in the region $0<y_*<2/\alpha_*$. This is

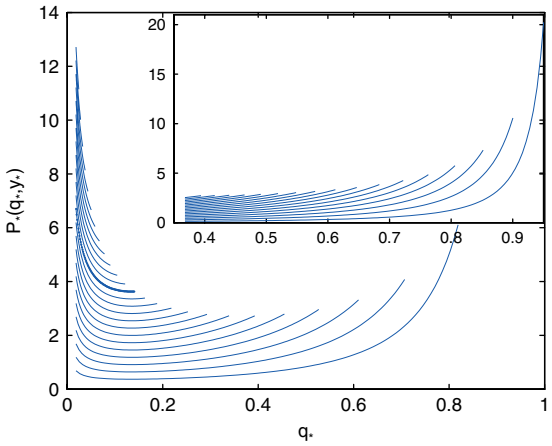

Figure 2. The behaviour of the smooth portion of $P_*(q_*, y_*)$ for two choices of α_*; we do not show the dry spike at $q_{\min}$. The major axes correspond to $\alpha_* = 4$; there is a transition from a bimodal to a unimodal PDF at $y_* = 2/\alpha_* = 0.5$. Larger y_* have smaller ranges of permissible q_*, and hence the curves are ordered such that y_* increases as we move to the left. The transition curve at $y_* = 2/\alpha_* = 0.5$ is shown by the dark line in the plot. The inset corresponds to $\alpha_* = 1$. The curves are ordered as in the main plot. In this case, counting the dry spike at $q_{\min}$, the PDF is bimodal at all values of y_*. This figure is available in colour online at wileyonlinelibrary.com/journal/qj

illustrated in Figure 2, which shows the smooth portion of P_* with $\alpha_* = 4$ and $\alpha_* = 1$. The PDF with $\alpha_* = 4$ changes from a bimodal to a unimodal form as one crosses $y_* = 2/\alpha_* = 0.5$. Indeed, for $y_* > 0.5$ the $\alpha_* = 4$ PDF falls monotonically from $q_* = \epsilon$. In the case with $\alpha_* = 1$, the PDF increases with increasing q_* at all values of y_*. Therefore, in combination with $\delta(q_* - \epsilon)$, the PDF is always bimodal if $\alpha_* < 2$.

On a middleworld isentrope, the saturation mixing ratio usually changes by more than an order of magnitude as one spans the entire midlatitudes, hence from (35) we expect that $\alpha_* > 2$ is the relevant atmospheric case. Therefore, close to the vapour source the PDF is bimodal. One mode, the dry spike $\delta(q - q_{\min})$, corresponds to a singularity at $q_{\min}$ after which the PDF falls off, only to rise again to a secondary moist peak as $q \to q_s(y)$. Further from the vapour source (i.e. for $y_* > 2/\alpha_*$) the PDF is unimodal, with a dry spike at $q_{\min}$ followed by a gradual monotonic decay to a minimum at $q = q_s(y)$.

We proceed to discuss the implications of the solution in (37) using dimensional variables. The non-dimensional versions of all formulae are obtained with $L \to 1$, $\alpha \to \alpha_*$ and $q_{\min} \to \epsilon$.

5.1. *Statistics in a strip $y_1 < y < y_2$*

The expressions in (36) and (37) provide the PDF at a specified y. From an observational and numerical view, recording the PDF at a particular y can be difficult. It is more likely that one obtains an estimate of the PDF over a strip, i.e. for $y \in [y_1, y_2]$. Integrating (37) over such a strip, and denoting this by $P_{12}(q)$, we have

$$P_{12}(q) = \int_{y_1}^{y_2} P(q, y)\, \mathrm{d}y\,, \\ = \left[\frac{\delta(q - q_{\min})}{2L^2} + \frac{\alpha}{2Lq \log^2(q/q_{\max})}\right] s_{12}(q)\,, \quad (41)$$

where the strip function is

$$s_{12}(q) = \begin{cases} y_2^2 - y_1^2 & \text{if } q_{\min} < q < q_s(y_2), \\ y_s^2(q) - y_1^2 & \text{if } q_s(y_2) < q < q_s(y_1). \end{cases} \quad (42)$$

The slightly complicated form of $s_{12}(q)$ results because when $q_s(y_2) < q < q_s(y_1)$ the upper limit of the integral is $y_s(q) < y_2$. We compare P_{12} above with the results of a Monte Carlo simulation in Figure 3.

The effect of the strip function s_{12} is to clip the secondary peak at $q = q_s$, and this clipping becomes more extreme if $y_2 - y_1$ is made larger. Thus, aggregating measurements of q from different spatial locations will obscure the bimodal structure of $P(q, y)$.

5.2. *The global PDF of q*

In the extreme case $y_1 \to 0$ and $y_2 \to L$, we obtain the global PDF of the specific humidity, denoted by $g(q)$, in (24). Using (25), the global PDF in this example is

$$g(q) = \frac{1}{2}\delta(q - q_{\min}) + \frac{1}{2\alpha L q}\,, \quad (43)$$

where $q \in [q_{\min}, q_{\max}]$. The smooth part of the global PDF is $g(q) \sim q^{-1}$.

5.3. *Monte Carlo simulations*

To test the analytic solution above, we proceed to a Monte Carlo simulation of our system. Typically our simulations use $N = 10^5$ parcels which are released in the domain $y \in [0, L]$. We have used $\alpha = 1, L = 5$ which gives $\alpha_* = 5$. This implies a change of approximately two orders of magnitude in the saturation specific humidity across the domain. The y-coordinates of the parcels are initially uniformly distributed and are tagged with the minimum saturated specific humidity, i.e. on parcel i, $q_i(0) = q_{\min}$. The parcels perform an uncorrelated random walk in y, and parcel i is reflected back into the domain if $y_i > L$ or $y_i < 0$. The forcing $\mathcal{S}$ is implemented by setting $q_i = q_{\max}$ when a parcel is reflected at $y = 0$. Rapid condensation is implemented by enforcing $q_i = \min[q_i, q_s(y_i)]$ after each random displacement.

To approximate Brownian motion, the root-mean-square step length of the random walk, ℓ, should be as small as is computationally feasible–we typically used $\ell = 2 \times 10^{-3} L$. We specify the Brownian diffusivity as $\kappa_b = 0.5$, and then the time between steps, τ, is computed via

$$\kappa_b = \frac{\ell^2}{2\tau}. \quad (44)$$

The simulation runs till $P(q, y)$ attains a stationary form and then data are collected in several strips for comparison with (41).

The results of the simulations are shown in Figure 3. The top panel of this figure shows a comparison between the smooth portion of the theoretical expression in (41) and the numerically estimated PDF for $y_* < 2/\alpha_*$. There is good agreement between the Monte Carlo simulation and the Fokker–Planck solution. Some minor discrepancies are evident as $q \to q_{\min}$; this is anticipated, as we have suppressed the numerical spike at $q = q_{\min}$ (indeed, the

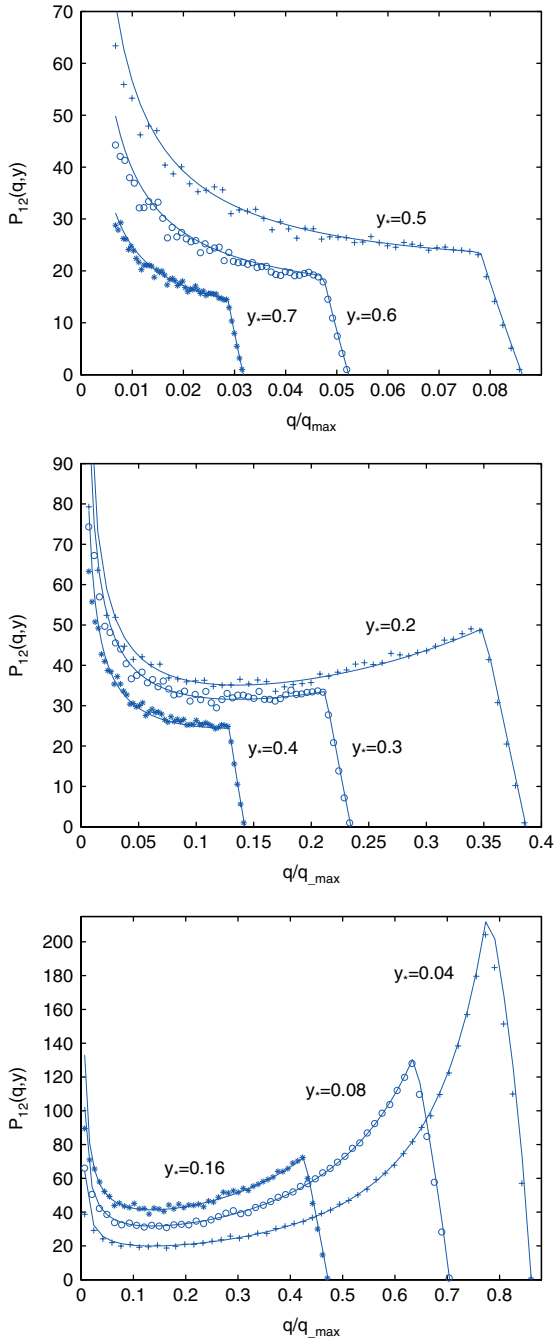

Figure 3. Comparison between $P_{12}(q, y)$ from Monte Carlo with the smooth portion of the analytic result in (41). In this illustration $\alpha_* = 5$. Crosses, open circles and stars are the Monte Carlo PDFs while the smooth solid curves are the analytical expression. Top panel: the bimodal PDFs for $y_* < 2/\alpha_*$. Middle panel: the PDFs for larger y_* which show the transition from a bimodal to a unimodal distribution. Bottom panel: the unimodal PDFs far from the source, i.e. for $y_* > 2/\alpha_*$. This figure is available in colour online at wileyonlinelibrary.com/journal/qj

theoretical PDF is given by a δ-function at this location). The middle panel of Figure 3 shows the PDF at larger y, specifically around the region where the PDF undergoes transition from a bimodal to a unimodal form. The bottom panel of Figure 3 shows the PDFs far from the source, where they have a single peak at $q = q_{\min}$ followed by decay and termination at $q = q_s(y)$. Finally, the first panel of Figure 4 shows the global PDF $g(q)$ in (43). As per the log–log inset, the global PDF closely follows the result in (43), with a spike at $q = q_{\min}$ followed by an algebraic tail $g(q) \sim q^{-1}$.

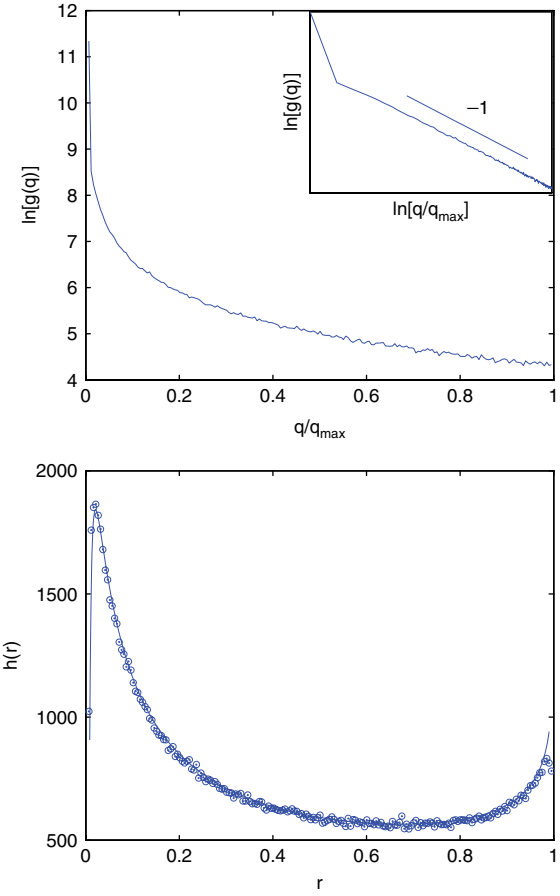

Figure 4. Top panel: the global PDF of the specific humidity $g(q)$ from Monte Carlo simulations. The inset shows a log–log plot, which reveals a spike at $q_{\min}$ followed by an algebraic q^{-1} tail as predicted by (43). Bottom panel: the analytical curve $h(r)$ from (51) (solid line) and the global RH PDF from the numerical simulation (dotted circles). This figure is available in colour online at wileyonlinelibrary.com/journal/qj

5.4. *Transport and condensation*

To understand the water-vapour distribution, it is important to quantify the transport of moisture. In the context of the AC model, it was shown by O'Gorman and Schneider (2006) that Brownian motion results in the mean moisture flux

$$\langle \mathcal{F} \rangle = -\kappa_b \frac{\mathrm{d}\langle q \rangle}{\mathrm{d}y}, \tag{45}$$

where $\langle q \rangle$ is the mean specific humidity and κ_b is the Brownian diffusivity. Then, as in (32), in a statistical steady state the convergence of $\langle \mathcal{F} \rangle$ balances the mean condensation $\langle \mathcal{C} \rangle$ at every y.

Using $f(q) = q$ in (29) and $q_s(y)$ in (35), the average gradient of specific humidity is obtained as

$$\frac{\mathrm{d}\langle q \rangle}{\mathrm{d}y} = \alpha q_{\max} \left[\mathrm{E}(\alpha L) - \mathrm{E}(\alpha y) \right], \tag{46}$$

where $\mathrm{E}(x) \stackrel{\mathrm{def}}{=} \int_x^\infty (\mathrm{e}^{-t}/t)\, \mathrm{d}t$ is the exponential integral. The moisture flux $\langle \mathcal{F} \rangle$ can also be diagnosed from the simulation and thus (45) is tested, with agreement shown in Figure 5.

5.5. *The relative humidity (RH)*

It is the immense subsaturation of the troposphere that makes the study of water vapour an interesting

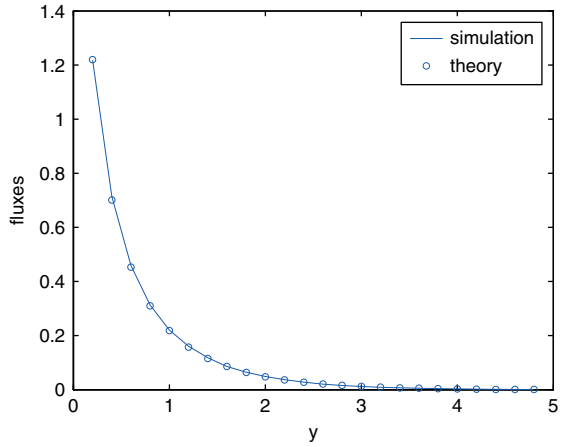

Figure 5. A comparison of the flux $\langle \mathcal{F} \rangle$ measured in the Monte Carlo simulation with the theoretical result using (45) and (46). This figure is available in colour online at wileyonlinelibrary.com/journal/qj

and challenging problem (Spencer and Braswell, 1997; Pierrehumbert *et al.*, 2005). This subsaturation is most starkly revealed by examining the RH, which is

$$r \stackrel{\text{def}}{=} \frac{q}{q_s(y)}\,. \tag{47}$$

Converting the PDF in (37) to a PDF for r, denoted by $Q(r, y)$, gives (for $y > 0$)

$$Q(r,y) = \frac{y}{L}\left[\frac{\delta(r - r_{\min})}{L} + \frac{\alpha}{r\log^2(\epsilon r/r_{\min})}\right], \tag{48}$$

where $r \in [r_{\min}(y), 1]$, ϵ is defined in (40) and

$$r_{\min}(y) = \epsilon e^{\alpha y}\,. \tag{49}$$

A comparison between (48) and the Monte Carlo simulation is shown in Figure 6. The main mismatch we see is for $r \to 1$, where the numerical PDFs taper off while expression (48) continues to rise till $r = 1$. This discrepancy is due to the collection of numerical data in a strip (as before), while (48) provides an expression for the PDF at a particular location. Note that the numerical PDFs show a spike at $r_{\min}(y)$–shown only in the first panel–which agrees with the shifting δ-function in (48). Bimodality of the PDF at small y is evident, while further from the source there is a peak at $r_{\min}(y)$ (suppressed in the plot), after which the PDF gradually levels off as $r \to 1$. The transition from a bimodal to a unimodal PDF, as well as the PDFs far from the source, are shown in the second and third panels of Figure 6 respectively.

5.6. *The global RH PDF*

The global PDF, $h(r)$, of RH is

$$h(r) \stackrel{\text{def}}{=} \int_0^{\log(r/\epsilon)/\alpha} Q(r,y)\mathrm{d}y. \tag{50}$$

Evaluating (50) using $Q(r, y)$ in (48) gives

$$h(r) = \frac{1}{\alpha L r}\log\left[\frac{\alpha L}{\log(1/r)}\right]. \tag{51}$$

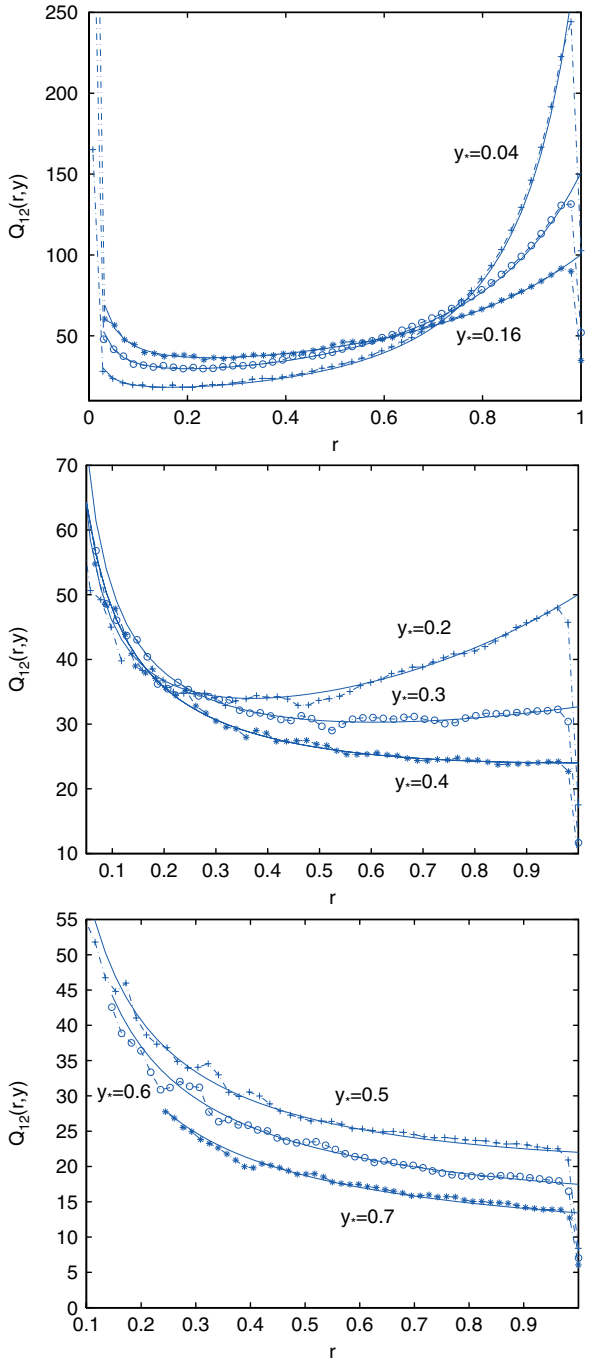

Figure 6. Comparison between $Q_{12}(r, y)$ from Monte Carlo with the smooth portion of the analytic result in (48). In this illustration $\alpha_* = 5$ and $y_2 - y_1 = 0.02L$. Crosses, open circles and stars are the Monte Carlo PDFs while the smooth solid curves are the analytical expression. Top panel: the bimodal PDFs for $y_* < 2/\alpha_*$ (the curve in the middle corresponds to $y_* = 0.08$). Middle panel: the PDFs for larger y_*, which show the transition from a bimodal to a unimodal distribution. Bottom panel: the unimodal PDFs far from the source, i.e. for $y_* > 2/\alpha_*$. This figure is available in colour online at wileyonlinelibrary.com/journal/qj

As a check, one can verify that on integration over the range of RH, that is $\epsilon \le r \le 1$, the global PDF in (51) normalizes to unity. The lower panel of Figure 4 shows a comparison between the Monte Carlo global RH PDF and (51). There is a good match between the theoretical prediction (50) and the simulation. The global PDF exhibits a mix of distinct features of the PDFs at different y, e.g. $h(r)$ is bimodal with a primary peak at small RH followed by a decay at intermediate RH and then a secondary 'moist peak' as $r \to 1$.

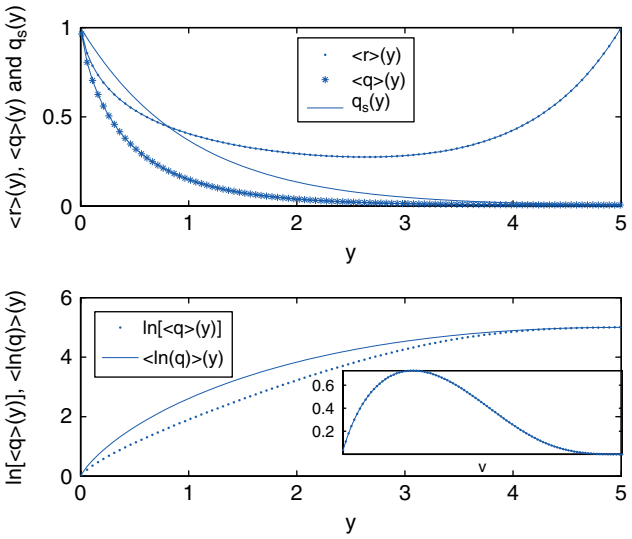

Figure 7. Upper panel: average profiles of the specific humidity and RH computed from the PDFs in (37) and (48) respectively. Lower panel: $\log\langle q\rangle(y)$ and $\langle\log(q)\rangle(y)$ as computed using (28). The inset shows the difference $\langle\log(q)\rangle(y) - \log\langle q\rangle(y)$ and demonstrates the increase in the OLR due to fluctuations in q at every y. This figure is available in colour online at wileyonlinelibrary.com/journal/qj

6. Discussion

6.1. *Radiative effects of water vapour*

In the Introduction, we referred to the importance of the vapour PDF in understanding the effect of humidity on the OLR. In fact, the effect of humidity on OLR was quantified by Zhang *et al.* (2003) in terms of the PDF of the RH field. Their numerical experiments, employing a full-fledged radiation code, showed that a domain with a bimodal RH PDF allowed for significantly larger cooling than one with a unimodal distribution (holding the total and mean the same in the two cases). In the present context, we see that the PDF of the RH over the domain, i.e. the lower panel of Figure 4, is bimodal. Therefore, along with regions of moderate RH, the domain consists of subsets with very small RH (the first peak in the aforementioned plot) and subsets that are nearly saturated (the second peak). A clearer picture is seen in the upper panel of Figure 7, which shows the average specific humidity and RH over the domain, i.e. $\langle q\rangle(y)$ and $\langle r\rangle(y)$ respectively. While the specific humidity decays monotonically from the source, the RH has a pronounced mid-domain minimum representing a pool of 'relatively' dry air flanked on either side by nearly saturated regions.

As described in PBR, the presence of water vapour affects the OLR in an approximately logarithmic fashion, i.e. OLR $\propto -\log(q)$. Therefore, the importance of knowing the PDF of q at every y is illustrated by comparing $\log(\langle q\rangle)$ with $\langle\log(q)\rangle$: it is the latter quantity that accounts for fluctuations in the specific humidity at every location and requires a knowledge of $P(q, y)$. As expected (see for example the discussion in PBR) and as shown in the lower panel of Figure 7[†] (especially the inset, which shows the difference between the two estimates), the fluctuations in the specific humidity field increase the OLR compared with the estimate based only on the mean profile $\langle q\rangle(y)$.

6.2. *Bimodality of the RH PDF*

It is interesting that the global PDF of q in the upper panel of Figure 4 is unimodal, while the global PDF of RH in the lower panel of Figure 4 is bimodal. Thus, according to our model, RH bimodality is so robust that it survives the mixing of PDFs from diverse locations into the global PDF $h(r)$ in (51).

As far as we are aware, bimodal RH PDFs that have been documented in literature are mostly derived from satellite data over the deep Tropics (Brown and Zhang, 1997; Zhang *et al.*, 2003; Mote and Frey, 2006; Luo *et al.*, 2007).

Exceptions are the three-dimensional and isentropic model-based AC experiments by PBR and Yang and Pierrehumbert (1994) respectively: in figure 16 in PBR and figure 6 of Yang and Pierrehumbert (1994) the midlatitude RH PDF is clearly bimodal.

On the other hand, the stochastic drying models developed by Sherwood *et al.* (2006) and Ryoo *et al.* (2009) predict only unimodal RH PDFs. Indeed, Sherwood *et al.* (2006) concluded that a broad and unimodal RH density might be regarded as a general outcome of the AC model. This conclusion is inconsistent with our implementation of the AC model, which results in bimodal RH PDFs. We discuss this point further in section 6.3.

Because our main focus is humidity fields on middleworld isentropic surfaces, we proceed with a data comparison by analyzing the RH on the 330 K isentropic surface as presented in the ERA interim product. The data were obtained from the European Centre for Medium-Range Weather Forecasts (ECMWF) web portal (http://data-portal.ecmwf.int/data/d/interim_daily/). We analyze daily data for the year 2008 given at a horizontal resolution of $1.5^\circ \times 1.5^\circ$ and at 24 vertical levels from 1000–175 mbar. As the RH data are only available at isobaric levels, we interpolate to generate RH fields on the 330 K isentrope. Further, as we are interested in the PDFs from the midlatitudinal portion of the isentropic surface, we collect data between 15° and 60° in both hemispheres.

A reviewer noted that the 330 K isentrope intersects the tropopause by 60°. To alleviate concerns that these bimodal PDFs result from sampling distinct air masses separated by a mixing barrier, we have also constructed PDFs by considering data only from the troposphere, for example, from 15° and 35° in both hemispheres, and verified that these PDFs display the same qualitative form as those in Figure 8.

As seen in Figure 8, which shows the PDFs from the different months of 2008 (PDFs from the individual hemispheres are plotted in the upper panel and a composite from both hemispheres is shown in the lower panel), there are considerable differences in the RH PDFs between the two hemispheres. For example, the dry peak in the PDFs is more prominent in each hemisphere's winter season. As these differences are not of primary interest to us we do not dwell on them here. There are a few values in the midlatitudes where the ERA dataset shows supersaturation; these have been set to 100% in the present calculation. Naturally, this raises the secondary peak but does not not alter the form of the PDF. Quite clearly, the PDF does vary from month to month but its main features are robust throughout the year.

[†]Both curves start at zero as we have chosen $q_{\max} = 1$; in general the value at $y = 0$ is $\log(q_{\max})$.

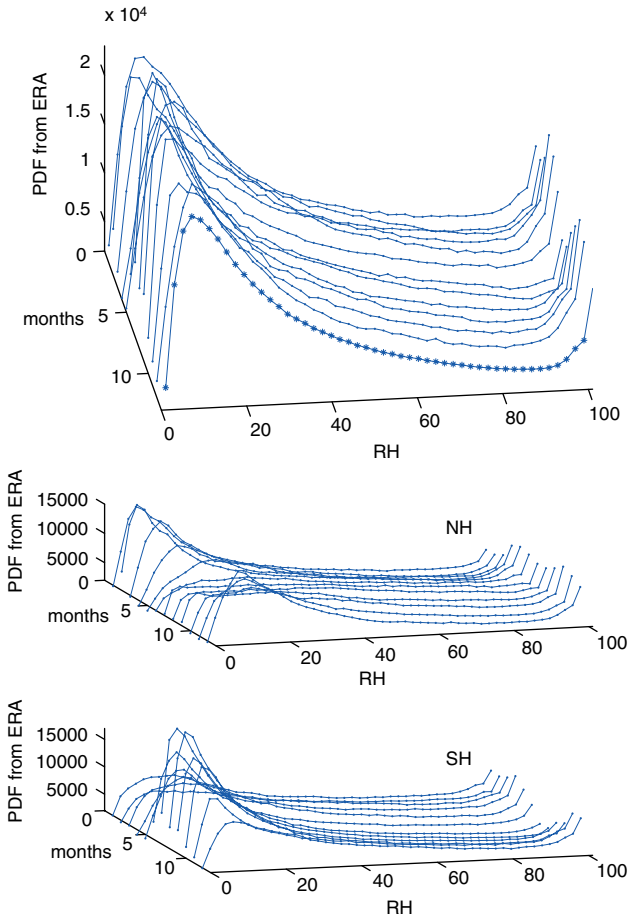

Figure 8. The midlatitudinal RH PDF on the 330 K isentrope as derived from the ERA interim data product for the individual months of 2008. Upper panel: PDFs from the two hemispheres plotted separately (ordering: from back to front January–December). Lower panel: lines with dots are the PDFs with both hemispheres taken together, and the foremost bold line with star symbols is the mean of these monthly curves. This figure is available in colour online at wileyonlinelibrary.com/journal/qj

More importantly, we observe that the ERA interim data PDF, in all months, is bimodal with distinct dry and moist peaks, which conforms with the results of the AC model in section 5.

6.3. *Special features of the AC model in this article*

In reconsidering the different ingredients in our idealized implementation of the AC model, we emphasize that there are at least four important assumptions affecting our conclusions:

- isentropic transport is modelled as Brownian motion;
- parcels are re-moistened only at $y = 0$;
- the saturation humidity is $q_s(y) = q_{\max} e^{-\alpha y}$;
- the model neglects diffusive processes.

The first assumption, which is equivalent to saying that the Lagrangian velocity correlation time is zero, is crucial for the derivation of the Fokker–Planck equation, and thus for all the results in this article. Moreover, following O'Gorman and Schneider (2006), we emphasize that the important condensation–diffusion balance in (32) also relies crucially on the assumption of Brownian motion. With non-zero velocity correlation time it might still be possible to argue that mean condensation $\langle \mathcal{C} \rangle$ is balanced by diffusive convergence, that is

$$\langle \mathcal{C} \rangle = \kappa_q \frac{\mathrm{d}^2 \langle q \rangle}{\mathrm{d}y^2} \,. \tag{52}$$

However, the humidity diffusivity κ_q will be systematically lower than the Brownian parcel diffusivity κ_b. Understanding the relation between κ_q and κ_b is beyond our scope here.

The second assumption of a localized vapour source probably explains the difference between our conclusions and those of Sherwood *et al.* (2006) regarding bimodality of the RH PDFs. This point could be examined within the Fokker–Planck framework by modelling the source $\mathcal{S}$ in (10) as a re-setting, $q \to q_s(y)$, occurring at a rate $\tau_{\text{Moist}}(y)$ throughout the domain. We do not pursue this generalization here.

The third assumption, that the saturation humidity varies exponentially with y, is a consequence of the Clausius–Clapeyron relation and the assumption that the temperature gradient on an isentrope is uniform. We have examined alternative models of $q_s(y)$, e.g. taking $q_s(y)$ as a linear or parabolic function of y while ensuring $q_s(y)$ is still monotonically decreasing $q_{\max}$ at $y = 0$. The main qualitative features of these solutions shown in Figures 3, 4 (lower panel) and 6 are unchanged. The only PDF that is sensitive to $q_s(y)$ is the global specific humidity PDF, $g(q)$, shown in the upper panel of Figure 4. Thus, compared with the q^{-1} algebraic decay in the exponential q_s, a linear (parabolic) saturation $q_s(y)$ yields a uniform (growing) PDF as $q \to q_{\max}$. These differences can be traced to the form of the function $y_s(q)$ in the analytic expression for $g(q)$ provided by (25).

The fourth assumption above is also crucial to the AC model. Haynes and Anglade (1997) estimate that in the upper troposphere and lower stratosphere the 'mix-down' time for synoptic-scale fluid parcels to be sheared and strained to molecular-diffusive scales is a few weeks. This time-scale is comparable to the mean residence time of water in the free troposphere (Quante and Matthias, 2006). Thus molecular diffusion between fluid parcels may have an impact on the water-vapour field, and in particular on its PDF. This important open question cannot be addressed till the advection–condensation model is extended to the advection–diffusion–condensation model.

7. Conclusions

We have studied the AC model forced by resetting the specific humidity at the southern boundary of the model isentrope. If the flow can be approximated by Brownian motion (i.e. a very rapidly decorrelating velocity), then the PDF of the vapour field is governed by the Fokker–Planck equation, which can be solved in the limit of rapid condensation. The solution is illustrated for a saturation profile that decays exponentially along the isentrope in the meridional direction. Analysis of this solution and supporting Monte Carlo simulations documents a non-trivial statistical steady state in which the southern moisture source is balanced by condensation throughout the interior of the domain. 'Non-trivial' refers to the fact that the steady state is far from the limiting states of complete saturation or complete dryness, and instead is characterized by a spatially inhomogeneous PDF. This non-uniformity manifests itself in the co-existence of very dry and nearly saturated regions within the domain. We find this to be encouraging, as a strongly inhomogeneous

steady state is reminiscent of the atmosphere. In fact, the bimodality of the global RH PDF predicted by the model is supported by midlatitudinal middleworld isentropic RH PDFs from the ERA interim product.

An important property of our solution is its spatial structure: near the resetting source (i.e. for small y) the PDF is bimodal with a peak at $q_{\min}$, a rapid decay followed by a rise to a second peak as $q \to q_s(y) \approx q_{\max}$. Further from the source (i.e. for large y) the PDF is unimodal and terminates at $q = q_s(y) \ll q_{\max}$. To facilitate a comparison with numerical experiments and observations we also derived an expression for the PDF as estimated over a strip of non-zero width. Extending the strip to cover the domain, we obtained the domain-averaged PDF, which in the case of an exponential saturation profile has a q^{-1} form. These features are in very good agreement with numerical simulations employing a large number of diffusively moving parcels. We also demonstrated the utility of the PDF in estimating mean field observables such as the moisture flux and condensation rate.

From the PDF of the specific humidity, we deduced the PDF of the RH. Once again, the PDFs near the source are bimodal with a peak at the minimum RH for a given y, i.e. at $r_{\min}(y)$, followed by a decay at intermediate RH values and a rapid rise as $r \to 1$. The bimodality gives way to a unimodal distribution at large distances from the source, and here the PDF is controlled by the δ-function at $r_{\min}(y)$, which levels off to a constant as $r \to 1$. The domain-averaged RH PDF displays a mix of these distinct features; in particular–even though the global specific humidity PDF is unimodal–the global RH PDF is bimodal with a primary peak at small RH followed by a decay at intermediate RH and then a secondary peak as $r \to 1$.

Though this work deals with an idealized model, we believe the analysis afforded in this setting provides a useful understanding of advection–condensation and the equilibria supported by the interaction of these processes with a steadily maintained source of moisture. Indeed, with a proper identification of the saturation profile and the resetting protocol, our methodology can be applied wherever the AC model finds use. Also, we argue that the algorithm outlined here is of practical interest in that, given a saturation profile from a general circulation model, one can then predict the form of the PDF of the vapour and relative humidity field. In turn, this can be compared with the PDFs generated directly from the model itself, thus providing a method to validate the fidelity of moisture evolution in a general circulation model.

Acknowledgements

WRY is supported by the NSF under Grant No. OCE07-26320. We thank Paul O'Gorman and Alexandra Tzella for a useful discussion of the AC model.

Appendix. Normalization as a differential boundary condition

Here we show that the normalization constraint obtained in the limit of rapid condensation can be interpreted as a differential boundary condition. Specifically, we consider this interpretation for the resetting problem and pick up the story at (18) where

$$P(q,y) = \frac{\Phi(q)}{L} + \left[\frac{\delta(q-q_{\min})}{L^2} + F(q)\right] y\,. \tag{A1}$$

Applying the normalization (15), for $y \in (0, L)$ we obtain

$$\frac{y}{L^2} + y\int_{q_{\min}}^{q_s(y)} F(q)\,\mathrm{d}q = \frac{1}{L}. \tag{A2}$$

Differentiating with respect to y, Leibnitz's rule gives

$$\frac{1}{L^2} + \int_{q_{\min}}^{q_s(y)} F(q)\mathrm{d}q + yF[q_s(y)]\,\frac{\mathrm{d}q_s}{\mathrm{d}y} = 0\,. \tag{A3}$$

A second differentiation yields

$$2F[q_s(y)]\frac{\mathrm{d}q_s}{\mathrm{d}y} + y\frac{\mathrm{d}F}{\mathrm{d}y}\left(\frac{\mathrm{d}q_s}{\mathrm{d}y}\right)^2 + yF[q_s(y)]\frac{\mathrm{d}^2q_s}{\mathrm{d}y^2} = 0\,. \tag{A4}$$

On specifying $q_s(y)$, we see that (A4) is an ordinary differential equation for the function $F(q)$. Indeed, (A4) is the interpretation of the normalization constraint as a differential boundary condition. To see the utility of (A4) in solving for $F(q)$, consider $q_s(y) = \mathrm{e}^{-\alpha y}$. This yields

$$[2 + \log(x)]F(x) + x\log(x)\frac{\mathrm{d}F(x)}{\mathrm{d}x} = 0 \tag{A5}$$

and hence $F(q) = \alpha/[Lq\log^2(q)]$, which agrees with the earlier result (37).

References

Brogniez H, Roca R, Picon L. 2009. Study of the free tropospheric humidity interannual variability using Meteosat data and an advection–condensation transport model. *J. Climate* **22**: 6773–6787.

Brown RG, Zhang C. 1997. Variability of midtropospheric moisture and its effect on cloud-top height distribution during TOGA COARE. *J. Atmos. Sci.* **54**: 2760–2774.

Fusi S, Mattia M. 1998. Collective behavior of networks with linear (VLSI) integrate-and-fire neurons. *Neural Computation* **11**: 633–652.

Galewsky J, Sobel A, Held I. 2005. Diagnosis of subtropical humidity dynamics using tracers of last saturation. *J. Atmos. Sci.* **62**: 3353–3367.

Haynes P, Anglade J. 1997. The vertical-scale cascade in atmospheric tracers due to large-scale differential advection. *J. Atmos. Sci.* **54**: 1121–1136.

Held I, Soden B. 2000. Water vapour feedback and global warming. *Ann. Rev. Energy Environ.* **25**: 441–475.

Luo Z, Kley D, Johnson RH. 1997. Ten years of measurements of tropical upper-tropospheric water vapor by MOZAIC. Part I: Climatology, variability, transport, and relation to deep convection. *J. Climate* **20**: 418–435.

Mote PW, Frey R. 2006. Variability of clouds and water vapor in low latitudes: View from Moderate Resolution Imaging Spectroradiometer (MODIS). *J. Geophys. Res.* **111**: D16101. DOI:10.1029/2005JD006791.

Neufeld Z, Haynes PH, Picard G. 2000. The effect of forcing on the spatial structure and spectra of chaotically advected passive scalars. *Phys. Fluids* **12**: 2506–2513.

O'Gorman PA, Schneider T. 2006. Stochastic models for the kinematics of moisture transport and condensation in homogeneous turbulent flows. *J. Atmos. Sci.* **63**: 2992–3005.

O'Gorman PA, Lamquin N, Schneider T. 2011. The relative humidity in an isentropic advection–condensation model: limited poleward influence and properties of subtropical minima. *J. Atmos. Sci.* (submitted).

Pierrehumbert RT. 1994. Tracer microstructure in the large-eddy dominated regime. *Chaos, Solitons and Fractals* **4**: 1091–1110.

Pierrehumbert RT. 1998. Lateral mixing as a source of subtropical water vapour. *Geophys. Res. Lett.* **25**: 151–154.

Pierrehumbert RT. 2002. The hydrologic cycle in deep-time climate problems. *Nature* **419**: 191–198.

Pierrehumbert RT. 2010. *Principles of Planetary Climate*. Cambridge University Press: Cambridge, UK.

Pierrehumbert RT, Roca R. 1998. Evidence for control of Atlantic subtropical humidity by large scale advection. *Geophys. Res. Lett.* **25**: 4537–4540.

Pierrehumbert RT, Brogniez H, Roca R. 2005. In *The General Circulation of the Atmosphere*, Schneider T, Sobel A (eds). Princeton University Press: Princeton, NJ.

Quante M, Matthias V. 2006. Water in the Earth's atmosphere. *J. Phys. IV* **139**: 37–61.

Ryoo J-M, Igusa T, Waugh DW. 2009. PDFs of tropical tropospheric humidity: measurement and theory. *J. Climate* **22**: 3357–3373.

Salathe E, Hartmann D. 1997. A trajectory analysis of tropical upper-tropospheric moisture and convection. *J. Climate* **10**: 2533–2547.

Schneider T, Smith KL, O'Gorman PA, Walker CC. 2006. A climatology of tropospheric zonal-mean water vapor fields and fluxes in isentropic coordinates. *J. Climate* **19**: 5918–5933.

Schneider T, O'Gorman PA, Levine X. 2010. Water vapor and the dynamics of climate changes. *Rev. Geophys.* **48**: RG3001, DOI:10.1029/2009RG000302.

Sherwood S. 1996. Maintainence of free-tropospheric tropical vater vapour distribution. Part II : Simulation by large scale advection. *J. Climate* **9**: 2919–2934.

Sherwood S, Kursinski ER, Read WG. 2006. A distribution law for free-tropospheric relative humidity. *J. Climate* **19**: 6267–6277.

Sherwood S, Roca R, Weckworth TM, Andronova NG. 2009. Tropospheric water vapour, convection and climate. *Rev. Geophys.* **48**: RG2001, DOI:10.1029/2009RG000301.

Soden B, Bretherton FP. 1993. Upper-tropospheric relative-humidity from the GOES 6.7 μm channel – method and climatology for July 1987. *J. Geophys. Res.* **98**: 16669–16688.

Spencer RW, Braswell WD. 1997. How dry is the tropical free troposphere? Implications for global warming theory. *Bull. Am. Meteorol. Soc.* **78**: 1097–1106.

Sukhatme J. 2005. Lagrangian velocity correlations and absolute dispersion in the midlatitude troposphere. *J. Atmos. Sci.* **62**: 3831–3836.

Wallace JM, Hobbs PV. 1977. *Atmospheric Science. An Introductory Survey*. Academic Press: San Diego, CA.

Yang H, Pierrehumbert RT. 1994. Production of dry air by isentropic mixing. *J. Atmos. Sci.* **51**: 3437–3454.

Zhang C, Soden B, Mapes B. 2003. Bimodality in tropical water vapour. *Q. J. R. Meteorol. Soc.* **129**: 2847–2866.

